

# Thermomechanical modeling of regressing heterogeneous solid propellants

K.R. Srinivasan<sup>c</sup>, K. Matouš<sup>a,\*</sup>, P.H. Geubelle<sup>c</sup>, T.L. Jackson<sup>b</sup>

<sup>a</sup> Department of Aerospace and Mechanical Engineering, University of Notre Dame, 367 Fitzpatrick Hall, Notre Dame, IN 46556, USA

<sup>b</sup> Computational Science and Engineering, University of Illinois at Urbana-Champaign, 1304 West Springfield Avenue, Urbana, IL 61801, USA

<sup>c</sup> Department of Aerospace Engineering, University of Illinois at Urbana-Champaign, 104 South Wright Street, Urbana, IL 61801, USA

## ARTICLE INFO

### Article history:

Received 21 November 2008

Received in revised form 29 June 2009

Accepted 5 July 2009

Available online 12 July 2009

### Keywords:

Thermomechanical model

Heterogeneous solid propellants

Generalized mixed finite element method

Lagrange multipliers

Bimaterial incompressible hyperelastic solids

## ABSTRACT

A numerical framework based on the generalized finite element method (GFEM) is developed to capture the coupled effects of thermomechanical deformations and thermal gradients on the regression rate of a heterogeneous solid propellant. The thermomechanical formulation is based on a multiplicative split of the deformation gradient and regression of the heterogeneous solid propellant is simulated using the level set method. A spatial mesh convergence study is performed on a non-regressing solid heterogeneous propellant system to examine the consistency of the coupled thermomechanical GFEM solver. The overall accuracy (spatial and temporal) of the coupled thermomechanical solver for regressing solid propellants is obtained from a periodic sandwich propellant configuration, where the effects of thermomechanical deformations on its regression rate is investigated. Finally, the effects of thermomechanical deformations in a regressing two-dimensional heterogeneous propellant pack are studied and time-average regression rates are reported.

© 2009 Elsevier Inc. All rights reserved.

## 1. Introduction

Heterogeneous solid propellants usually consist of highly loaded composites made of energetic particles embedded in a soft incompressible elastomeric binder. Of particular interest in this study are AP/HTPB propellants composed of very stiff Ammonium Perchlorate (AP) particles embedded in a soft elastomeric Hydroxyl-Terminated-Poly-Butadiene (HTPB) binder (Fig. 1). In a steadily regressing solid propellant, stresses and temperatures sufficiently far away from the propellant surface are relatively uniform. However, close to the propellant surface, i.e., within the thermal boundary layer, thermal conduction within the solid generates steep thermal gradients that give rise to large thermomechanical strains. Heterogeneity of the solid propellant results in differential thermal expansions and regions of high stress concentrations across AP/HTPB interfaces. In some scenarios, the AP/Binder interface may experience tensile stresses that lead to debonding which may affect the regression phenomena and sometimes lead to catastrophic failure [3].

A majority of the experimental and theoretical studies investigating the effect of deformation on propellant regression have been performed predominantly on pre-cracked *macroscopic* solid propellant specimens. Kumar et al. [4,5] observed an increase in pressure near the crack front with an increase in crack length and Kuo et al. [6] observed crack branching at high pressurization rates. Recently, Berghout et al. [3] carried out a comprehensive study on the *macroscopic* effect of damage on the propellant surface regression. They conclude that a minimum *macroscopic* crack width is required to cause any significant change in propellant regression rate. However, to our knowledge there has been no experimental effort that has studied the effect of *microscopic* deformations on propellant regression, within the thermal boundary layer. Kuznetsov

\* Corresponding author. Tel.: +1 574 631 1376; fax: +1 574 631 6855.

E-mail address: [kmatous@nd.edu](mailto:kmatous@nd.edu) (K. Matouš).

URL: <http://www.nd.edu/~kmatous> (K. Matouš).

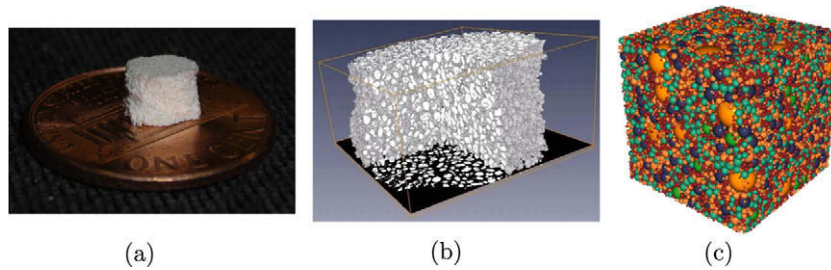


**Fig. 1.** Heterogeneous solid propellant; (a) sample of heterogeneous solid propellant [1]; (b) tomographic image of the complex microstructure [1]; and (c) computer generated pack used in numerical modeling [2].

and Stewart [7] carried out one-dimensional theoretical and numerical studies to determine the effect of thermal expansion and variable thermal properties on regression rates of a *homogeneous* solid propellant within the thermal boundary layer and observed that the thermal expansion results in a regression rate decrease.

The numerical treatment of regressing heterogeneous solid propellants pose several challenges. The first one is the accurate representation and discretization of the heterogeneous microstructure, especially for high loadings of AP (Fig. 1). Recent advances in the generalized finite element method (GFEM) [8–12] have provided a novel approach to tackle this complexity wherein the finite element mesh does not have to conform to the microstructure. The second challenge associated with the modeling of solid propellants arises from significant differences (with the AP particles about 4000 times stiffer than the binder) in stiffness between AP and HTPB binder and from the nearly-incompressible nonlinear material behavior of the binder. Yet another difficulty is the accurate modeling of the complex combustion processes responsible for ignition and propagation of the propellant flame that causes steady propellant regression. Furthermore, regressing heterogeneous solid propellant surfaces are seldom planar and undergo complex topological changes. Evolving topologies have been successfully modeled by the level set method [13]. In particular, Wang et al. [14–16] have developed level set-based methods capable of simulating two- and three-dimensional combustion of heterogeneous solid propellants in the absence of thermomechanical deformation. Finally, large thermal expansions near the propellant surface lead to significant changes in shape and curvature that influence thermal conduction. Therefore, coupled effects of thermal conduction and thermomechanical deformations have to be considered simultaneously.

The objective of the present work is to develop a numerical framework, based on the generalized finite element method, capable of simulating regression of heterogeneous solid propellants experiencing large thermomechanical strains. In this paper, we present a thermomechanical formulation based on the multiplicative split of the deformation gradient and a level set-based surface regression model for heterogeneous propellants. In our previous work [12], we have formulated and tested a generalized mixed finite element method to simulate the (isothermal) mechanical deformations in highly disparate heterogeneous material systems with nearly-incompressible behavior. In this paper, we extend the generalized mixed finite element method to accommodate both thermomechanical deformations and evolving surface topologies in propellant regression problems. We adopt an approach similar to Ji et al. [17] where dynamics of thermally induced swelling of compressible gels was investigated using the *assumed gradient* level set method [18].

In this introductory study, we do not introduce the complex combustion reactions at the propellant surface and the resulting transport of the product gases [14,19,20]. Instead, we assume that the heat generated by the gaseous products is constant and is applied along the propellant surface as a simple heat flux. We assess the spatial and temporal convergence properties of the proposed numerical method using a periodic sandwich propellant problem [19] and investigate the effect of deformation on the regression of both periodic sandwich propellants and heterogeneous propellant packs.

The remainder of the paper is organized as follows: in Section 2.2, the governing equations for the regression of a heterogeneous solid propellant are summarized, followed in Section 3 by the derivation of a weak formulation of these equations. The generalized finite element approximations, in the context of a mixed method, and the level set method for propellant regression are discussed in Section 4. Section 5 describes the convergence test employed to assess the numerical methodology derived for thermomechanical deformations and examples of regression of two-dimensional sandwich and heterogeneous propellant packs are presented to demonstrate the efficacy of the method.

In this paper, we denote second-order tensors with uppercase boldface Roman letters, e.g.  $\mathbf{F}$  and vectors in a reference configuration with capital boldface italic Roman letters  $\mathbf{Q}$ , while other vectors are denoted by lowercase boldface italic Roman and Greek letters, e.g.  $\mathbf{u}$  and  $\lambda$ . Fourth-order tensors are denoted using the calligraphic font, e.g.  $\mathcal{A}$ .

## 2. Thermomechanical model for propellant regression

Let  $\varphi : \Omega_0(t_0) \rightarrow \Omega_0(t)$  represent the regression of a heterogeneous solid propellant surface  $\Gamma_1^0$  in the time interval  $(t_0, t)$  and let the domain  $\Omega_0$  be composed of solid  $\Omega_0^s$  and fluid  $\Omega_0^f$  regions separated by the solid–fluid interface  $\Gamma_1^0$ , as illustrated in Fig. 2. The domain  $\Omega_0^s$  represents a  $N$ -phase heterogeneous solid propellant ( $\Omega_0^s = \bigcup \mathcal{B}_i^s$ ,  $i = 1 \dots N$ ) system, while  $\Omega_0^f$  represents the phase consisting of gaseous products released by combustion processes at the propellant surface  $\Gamma_1^0$ . In addition to

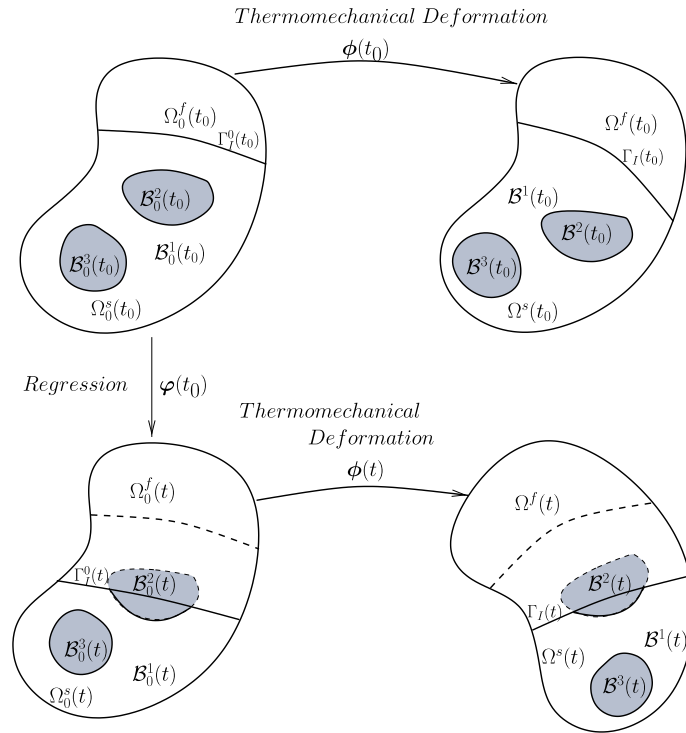


**Fig. 2.** Schematic of regression of heterogeneous solid propellant system  $\Omega_0$  composed of solid and gaseous phases ( $\Omega_0^s, \Omega_0^f$ ) separated by an interface  $\Gamma_1^0$ .  $\Omega_0$  and  $\Omega$  represent the reference and deformed configurations of the propellant.

the solid–fluid interface  $\Gamma_1^0$ , solid–solid interfaces  $S_0$  separate the solid phase  $\Omega_0^s$  into its constituents (AP particles and HTPB matrix). Unlike the regressing solid–fluid interface  $\Gamma_1^0$ , the solid–solid interface  $S_0$  remains stationary.

The regression of the propellant surface  $\Gamma_1^0$  depends on the local surface temperature and hence requires accurate resolution of the temperature field. The regression phenomena are also influenced by deformations on the propellant surface caused by large thermal gradients in the vicinity of the interface  $\Gamma_1^0$ . Therefore, an accurate description of the regression phenomena entails solution of temperature and deformations simultaneously. In the present study, we restrict our attention to solution of temperature and thermomechanical deformations in the solid phase  $\Omega_0^s$  alone, and assume the flow of heat  $Q^f$  from the fluid phase  $\Omega_0^f$  into the solid phase to be a constant.

The multi-physics nature of this problem naturally raises the question about the relevant length and time scales. This issue has been addressed previously in the work of Hegab et al. [19], who report that the typical length and time scales for the gas phase (not considered in this work) are  $L_g = 3.10 \mu\text{m}$  and  $t_g = 1.36 \times 10^{-6} \text{s}$ , while those of the solid phase are  $L_s = 27.8 \mu\text{m}$ ,  $t_s = 2.80 \times 10^{-3} \text{s}$ , respectively. Finally, the length and time scales for the interface are  $L_i = 20.1 \mu\text{m}$  and  $t_i = 2.00 \times 10^{-3} \text{s}$ . These length and time scales provide characteristic wave speeds for a thermal wave in the solid phase,  $c_T = 0.01 \text{m/s}$ , and the regression rate,  $r_b = 0.01 \text{m/s}$ . One should also assume elastic longitudinal and shear waves governed by  $c_l = \sqrt{E/\rho}$  and  $c_s = \sqrt{\mu/\rho}$ , where  $E$  represents Young’s modulus and  $\mu$  denotes the shear modulus, respectively. Assuming the properties of a more compliant blend presented in Section 5, we get  $c_l = 88 \text{m/s}$  and  $c_s = 51 \text{m/s}$ . As expected, the thermal wave speed and the regression rate are of a similar order, and thus, must be resolved concurrently. On the other hand, the elastic waves are approximately 5000 times faster and are therefore neglected in this work.

With the length and time scales discussed above in mind, we outline in this section the governing equations that describe the thermomechanical deformation and temperature fields. In addition, the regression of the heterogeneous solid propellant surface  $\Gamma_1^0$  using a level set method [13] is also described.

### 2.1. Kinematics

The heterogeneous solid propellant  $\Omega_0^s$ , as shown in Fig. 3, is assumed to be a multi-material hyperelastic body in an initial configuration  $\mathcal{B}_0 \subset \mathbb{R}^3$  and homogeneous reference temperature  $\theta_0(\mathbf{X}, t)$  that undergoes a motion  $\phi(\mathbf{X}, t)$  and change in internal energy to the current configuration  $\mathcal{B} \subset \mathbb{R}^3$  at a temperature  $\theta(\mathbf{x}, t)$ . Here  $\mathbf{X}$  and  $\mathbf{x} \in \mathbb{R}^3$  designate the position of a particle in the reference  $\mathcal{B}_0$  and current  $\mathcal{B}$  configuration, respectively. Let  $\mathbf{F}(\mathbf{X}, t) = \nabla_{\mathbf{X}}\phi(\mathbf{X}, t)$  be the deformation gradient at the current time  $t \in \mathbb{R}^+$  with the Jacobian given by  $J = \det(\mathbf{F})$ , and let  $\mathbf{C} = \mathbf{F}^T\mathbf{F}$  be the right Cauchy–Green tensor, then the displacement vector  $\mathbf{u}$  is obtained from  $\mathbf{x} = \mathbf{X} + \mathbf{u}$ .

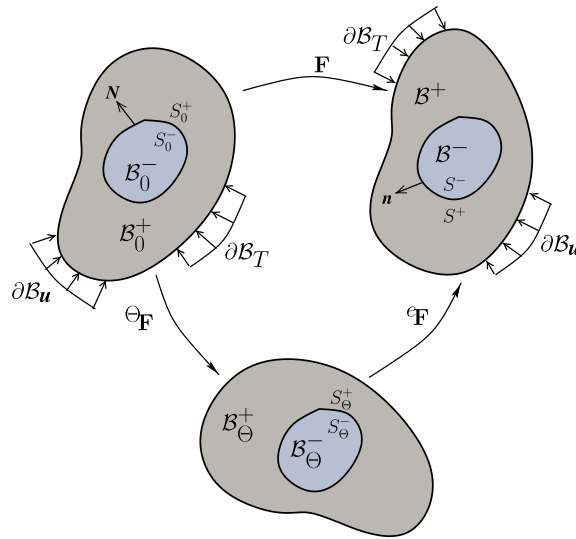


Fig. 3. Illustration of the mapping of a bimaterial system from  $B_0$  to  $B$  through an intermediate stress-free configuration  $B_\theta$ .

Without loss of generality, the heterogeneous solid propellant is considered to be a bimaterial system in the description that follows. Suppose now that the body  $B_0$ , with a homogeneous reference temperature of  $\theta_0$ , is divided by a material interface  $S_0$  with a unit normal  $N$ . We assume that the material interface partitions the body into two subbodies  $B_0^\pm$ , occupying the plus and minus sides of the material interface,  $S_0^\pm$ , respectively. The deformation on either side of the interface is denoted by  $\phi^\pm : B_0^\pm \rightarrow B^\pm$ . The mapping  $F$  is further decomposed multiplicatively into a volume change associated with free thermal expansion/contraction  ${}^\theta F$  and a stress-producing isothermal deformation  ${}^e F$  [21,22], as shown in Fig. 3,

$$F = {}^e F {}^\theta F. \tag{1}$$

The intermediate configuration  $B_\theta$  is assumed to be isolated from the body and is obtained through a stress-free volumetric expansion/contraction of  $B_0$  subjected to a relative temperature field  $\Delta\theta = \theta - \theta_0$ . For inhomogeneous deformation and temperature fields, the mappings from  $B_0$  to  $B_\theta$  and  $B_\theta$  to  $B$  need not be continuous one-to-one mappings, and the total deformation  $F$  is the only true deformation gradient. An arbitrary rigid-body rotation superposed to  $B_\theta$  will yield another stress-free intermediate configuration resulting in a non-unique decomposition (1). Therefore, we specify a unique decomposition for thermally isotropic solids with a thermal deformation gradient  ${}^\theta F$  given by

$${}^\theta F = \beta(\theta)\mathbf{1}, \tag{2}$$

where  $\beta$  represents the stretch ratio in any material direction and  $\mathbf{1}$  is the second-order identity tensor. The linearized form of the thermal stretch ratio  $\beta$  is a function of the coefficient of linear thermal expansion  $\tilde{\alpha}$  given by

$$\beta(\theta) = \exp \left[ \int_{\theta_0}^{\theta} \tilde{\alpha} d\theta \right] \simeq 1 + \tilde{\alpha}(\theta - \theta_0). \tag{3}$$

### 2.2. Governing equations

In this section, we derive the governing equations for thermomechanical deformations and temperature field in the solid propellant. The multiplicative decomposition of the deformation gradient  $F$  enables an additive split of the Helmholtz free energy  $\psi$  [21,22] given by

$$\psi = {}^e \psi({}^e F, \theta) + {}^\theta \psi(\theta), \tag{4}$$

where  ${}^e \psi$  is a hyperelastic strain energy potential that depends on the deformation gradient  ${}^e F$  and temperature  $\theta$ , while  ${}^\theta \psi$  is a thermal potential that depends on temperature  $\theta$  alone. Particular choices of  ${}^e \psi$  and  ${}^\theta \psi$  that yield governing equations and constitutive laws for the solution of thermomechanical deformations and temperature field are described in Sections 2.2.1 and 2.2.2, respectively.

#### 2.2.1. Thermomechanical formulation

To accommodate significant difference in material shear and bulk response of the binder, the deformation gradient  ${}^e F$  is decomposed into a dilatational/volumetric and a deviatoric/isochoric part. The volume-preserving part of the deformation gradient  ${}^e F$  is given by

$${}^e\widehat{\mathbf{F}} = {}^eJ^{-\frac{1}{3}}{}^e\mathbf{F}, \tag{5}$$

while an independent variable  $\gamma$  is used to capture the volumetric response,

$$\gamma = {}^eJ, \tag{6}$$

and we introduce  ${}^e\overline{\mathbf{F}} = \gamma^{\frac{1}{3}}{}^e\widehat{\mathbf{F}}$  as a mixed deformation gradient with  $\overline{\mathbf{F}} = {}^e\overline{\mathbf{F}}{}^e\mathbf{F}$ . Note that, in the finite element formulation that follows, (6) is enforced in a weak sense.

In this study,  ${}^e\psi$  is the neo-Hookean strain energy functional  ${}^eW$  composed of distortional  ${}^e\widehat{W}$  and dilatational  ${}^eU$  parts as in [12],

$$\rho_{\Theta} {}^e\psi({}^e\mathbf{F}, \Theta) = {}^eW\left(\gamma^{\frac{1}{3}}{}^e\widehat{\mathbf{F}}\right) = {}^e\widehat{W}({}^e\mathbf{F}) + {}^eU(\gamma), \tag{7}$$

and the first Piola–Kirchhoff stress tensor  $\mathbf{P}$  defined on  $\mathcal{B}_0$  is given by

$$\mathbf{P} = \frac{\rho_0}{\beta^2} {}^e\overline{\mathbf{F}} \frac{\partial {}^e\psi}{\partial {}^e\mathbf{F}} \Big|_{\mathbf{F} = {}^e\overline{\mathbf{F}}}, \tag{8}$$

with  $\rho_0$  and  $\rho_{\Theta}$ , ( $\rho_0 = {}^eJ\rho_{\Theta}$ ), being the densities at the reference and intermediate configurations  $\mathcal{B}_0$  and  $\mathcal{B}_{\Theta}$ , respectively. By selecting proper potential functions,  ${}^e\widehat{W}$  and  ${}^eU$ , we can model both compressible and nearly-incompressible solids.

Upon imposition of quasi-static equilibrium and boundary conditions, we obtain the governing equations for thermomechanical deformations in the reference configuration  $\mathcal{B}_0$  as

$$\begin{aligned} \nabla_{\mathbf{x}} \cdot \mathbf{P} + \mathbf{b}_0 &= \mathbf{0} && \text{in } \mathcal{B}_0^{\pm}, \\ \mathbf{P} \cdot \mathbf{N} &= \underline{\mathbf{t}}_0 && \text{on } \partial\mathcal{B}_T, \\ \llbracket \mathbf{P} \cdot \mathbf{N} \rrbracket &= \mathbf{0} && \text{on } S_0^{\pm}, \\ \phi &= \phi_p && \text{on } \partial\mathcal{B}_u, \end{aligned} \tag{9}$$

where  $\llbracket \cdot \rrbracket$  is the jump operator,  $\mathbf{N}$  is the unit normal in the reference configuration,  $\mathbf{b}_0$  is the body force vector acting per unit volume of  $\mathcal{B}_0^{\pm}$ ,  $\underline{\mathbf{t}}_0$  is the externally applied traction vector on  $\partial\mathcal{B}_T$ , and  $\phi_p$  is the externally applied displacement vector on  $\partial\mathcal{B}_u$ , with  $\partial\mathcal{B}_T \cap \partial\mathcal{B}_u = \emptyset$ .

### 2.2.2. Thermal conduction

To derive the governing equation that describes the temperature field in the solid propellant, we assume the purely thermal part of the Helmholtz free energy  ${}^{\Theta}\psi$  to be

$${}^{\Theta}\psi = c(\Theta - \Theta_0) - c\Theta \ln \frac{\Theta}{\Theta_0}, \tag{10}$$

where  $c$  is the specific heat at constant deformation (volume). The specific entropy  $\eta$  satisfies the Gibbs relation:

$$\eta = -\frac{\partial \psi}{\partial \Theta} \Big|_{\mathbf{F}}. \tag{11}$$

Next, we write a standard energy balance equation in the spatial configuration

$$\dot{e}_c = \boldsymbol{\sigma} : \mathbf{d} - \text{div} \mathbf{q} + r, \tag{12}$$

where  $e_c$  is the internal energy in the current configuration,  $\boldsymbol{\sigma} = 1/J\mathbf{P}\mathbf{F}^T$  is the Cauchy stress tensor,  $\mathbf{d}$  denotes the rate of deformation tensor and  $r$  represents the heat source. For the small strain rates present in this investigation, we neglect the stress power, as typical for hyperelastic materials under the quasi-static loading. Upon neglecting the dissipative microstructural changes caused by thermoelastic deformation and the associated entropy production, the rate of specific entropy  $\eta$  caused by heat flow is given by

$$\Theta \dot{\eta} = \frac{1}{\rho} \nabla_{\mathbf{x}} \cdot \mathbf{q}. \tag{13}$$

The spatial heat flux  $\mathbf{q}$  in the current configuration  $\mathcal{B}$  is modeled using Fourier’s law,

$$\mathbf{q} = -\Lambda(\Theta) \nabla_{\mathbf{x}} \Theta \quad \text{in } \mathcal{B}^{\pm}, \tag{14}$$

where the temperature dependent thermal conductivity  $\Lambda > 0$ . Note that  $\mathbf{q}$  satisfies the *Clausius-Duhem* inequality  $\mathbf{q} \cdot \nabla_{\mathbf{x}} \Theta \leq 0$  on either side of the material interface  $S$ . Here  $\nabla_{\mathbf{x}}$  represents the spatial deformation gradient given by  $\nabla_{\mathbf{x}}(\cdot) = \nabla_{\mathbf{X}}(\cdot) \mathbf{F}^{-1}$ . The nominal heat flux vector  $\mathbf{Q}$  in the reference configuration  $\mathcal{B}_0$  is obtained by performing a pull-back of the spatial heat flux vector,  $\mathbf{q}$ ,

$$\mathbf{Q} = -J\Lambda(\Theta) \mathbf{C}^{-1} \nabla_{\mathbf{X}} \Theta \quad \text{in } \mathcal{B}_0^{\pm}, \tag{15}$$

and the nominal heat flux vector  $\mathbf{Q}$  satisfies the *Clausius-Duhem* inequality  $\mathbf{Q} \cdot \nabla_{\mathbf{x}} \theta \leq 0$  as well. Combining Eqs. (10), (11) and (13), we obtain the governing equation for temperature  $\theta$  in the reference configuration as

$$\begin{aligned} \rho_0(\mathbf{X}, t) c \dot{\theta}(\mathbf{X}, t) - \nabla_{\mathbf{x}} \cdot \mathbf{Q} &= 0 && \text{in } \mathcal{B}_0^\pm, \\ \llbracket \mathbf{Q} \cdot \mathbf{N} \rrbracket &= 0 && \text{on } S_0, \\ \theta &= \theta^p && \text{on } \partial \mathcal{B}_\theta, \\ \mathbf{Q} &= \mathbf{Q}^p && \text{on } \partial \mathcal{B}_p, \end{aligned} \quad (16)$$

where  $\rho_0(\mathbf{X}, t) = J\rho(\mathbf{x}, t)$ ,  $\theta^p$  is the applied temperature field on boundary  $\partial \mathcal{B}_\theta$  and  $\mathbf{Q}^p$  is the applied heat flux on boundary  $\partial \mathcal{B}_p$ .

### 2.3. Propellant regression

The propellant regression is modeled using an *assumed gradient* level set method [18], where the propellant surface is represented as the zero level set of a scalar function  $\phi^l(X, t)$  [13,14].

In the present study, the propellant surface is evolved in time using the modified level set advection equation

$$\dot{\phi}^l(\mathbf{X}, t) + v_e(\mathbf{X}, t) = 0 \quad \text{in } \Omega_0, \quad (17)$$

where  $v_e(\mathbf{X}, t)$ , commonly referred to as the *extension velocity* [23,24], physically represents the local regression rate on the propellant surface closest to the point  $\mathbf{X}$ . For heterogeneous solid propellants, the extensional velocity  $v_e$  along the propellant surface ( $\phi^l = 0$ ) is the same as the local surface regression rate  $r_b$ , i.e.,

$$v_e|_{\phi^l=0} = r_b. \quad (18)$$

A simple pyrolysis law is used to relate the surface regression rate  $r_b$  to the surface temperature  $T_s$ ,

$$r_b = A \exp(-E_a/RT_s), \quad (19)$$

where  $E_a$  is the activation energy,  $A$  is the Arrhenius constant, and  $R$  is the universal gas constant. Note that we do not use the level set method to capture the discontinuity. The discontinuity is captured by the GFEM. Level set is used only to describe the geometry of the front and its motion, not the resulting discontinuities in displacement and temperature gradients.

### 2.4. Propellant surface jump conditions

The jump conditions at the propellant surface relate the solution in the solid phase  $\Omega_0^s$  to the fluid/gas phase  $\Omega_0^f$ . As mentioned in Section 2.2, we numerically resolve thermomechanical deformation and temperature in the solid phase  $\Omega_0^s$  alone, and assume the normal heat flux generated in the fluid phase to be a constant  $Q_f$  acting along the solid–fluid interface  $I_1^0$ . The balance of normal heat fluxes across the solid–fluid interface  $I_1^0$  yields

$$\llbracket \mathbf{Q} \cdot \mathbf{N} \rrbracket = (Q_f - Q_s) = -q^s M, \quad (20)$$

where the mass flux  $M$  ejected from the solid phase at the propellant surface is a function of the local regression rate  $r_b$  (19) and is given by

$$M = \rho_s r_b = \rho_s A \exp(-E_a/RT_s). \quad (21)$$

Note that  $r_b$ ,  $\rho_s$  and  $q^s$  take on different values for the AP and the binder with  $q^s > 0$  ( $< 0$ ) for exothermic (endothermic) processes. The heat added into the solid phase  $Q_s$  evaluated from (20) and (21) is

$$Q_s = Q_f + q^s \rho_s A \exp(-E_a/RT_s). \quad (22)$$

It is evident from (22) that the heat added to the solid phase at the propellant surface is dependent on the local surface temperature  $T_s$ , thereby rendering the initial value problem (16) nonlinear.

## 3. Weak formulation

For completeness and clarity of presentation, we summarize here the weak formulations of the governing equations (9) and (16). The motion of the body  $\phi^\pm$  governed by (9) is based on a Discontinuous Deformation Map (DDM) method that admits jumps in primary fields as well as its gradients, with the continuity of the primary fields enforced weakly [12]. A similar approach is adopted for (16) where jumps in both the temperature and its gradient are admitted and the continuity of temperature is again enforced weakly.

### 3.1. Thermomechanical deformations

The de Veubeke-Hu-Washizu variational statement of the thermomechanical governing equations (9) in the reference configuration reads

$$\Pi(\phi, p, \gamma, \lambda) = \int_{B_0^\pm} \theta J \left\{ {}^e \widehat{W}(\mathbf{F}^\theta \mathbf{F}^{-1}) + {}^e U(\gamma) \right\} dV_0 + \int_{B_0^\pm} \theta J p (J - \gamma) dV_0 + \int_{S_0} \lambda \cdot \llbracket \phi \rrbracket dS_0 + \Pi_{\text{ext}}, \tag{23}$$

where  $p$  is the pressure and  $\lambda$  is the Lagrange multiplier vector that enforces continuity of the deformation maps  $\phi^\pm$ , i.e., the interface tractions.  $\Pi_{\text{ext}}$  is the total potential energy associated with body forces  $\mathbf{b}_0$  and externally applied tractions  $\mathbf{t}_0$ . For isotropic thermal expansion described by (2) and  $\theta J = \beta^3(\theta)$ , the stationarity condition of (23) gives

$$\begin{aligned} \delta \Pi(\phi, p, \gamma, \lambda) &= \int_{B_0^\pm} \beta^2 \widehat{\mathbf{P}} : \delta \mathbf{F} dV_0 + \int_{B_0^\pm} \beta^3 U'(\gamma) \delta \gamma dV_0 + \int_{B_0^\pm} \delta p (J - \gamma \beta^3) dV_0 + \int_{B_0^\pm} p (\delta J - \delta \gamma \beta^3) dV_0 + \int_{S_0} \delta \lambda \cdot \llbracket \phi \rrbracket dS_0 \\ &+ \int_{S_0} \lambda \cdot \llbracket \delta \phi \rrbracket dS_0 + \delta \Pi_{\text{ext}} = 0 \end{aligned} \tag{24}$$

for all admissible variations

$$\begin{aligned} \delta \mathbf{u} &\in [H^1(B_0)], \quad \delta \mathbf{u} = \mathbf{0} \quad \text{on } \partial B_{\mathbf{u}}, \\ \delta p &\in L_2(B_0), \quad \delta \gamma \in L_2(B_0), \\ \delta \lambda &\in [H^{-\frac{1}{2}}(S_0)], \end{aligned} \tag{25}$$

where  $\widehat{\mathbf{P}} = \partial^e \widehat{W}(\mathbf{F}) / \partial^e \mathbf{F}$  and  $H^1(B_0)$  is the Sobolev space of square-integrable functions with weak derivatives up to first-order with range in  $\mathbb{R}^3$ .

### 3.2. Thermal conduction

The variational form of (16), in conjunction with a weak enforcement of temperature continuity across the material interface  $S_0$  through Lagrange multipliers, is obtained through a weighted Galerkin method that yields the following mixed variational form:

$$\int_{B_0^\pm} \delta \theta \rho_0 c \dot{\theta} dV_0 + \int_{B_0^\pm} \nabla_{\mathbf{x}} \delta \theta \cdot \mathbf{Q} dV_0 + \int_{S_0} \bar{\lambda} \llbracket \delta \theta \rrbracket dS_0 + \int_{S_0} \delta \bar{\lambda} \llbracket \theta \rrbracket dS_0 = \int_{\partial B_p} \delta \theta \mathbf{Q}^p \cdot \mathbf{N} d\partial B_p \tag{26}$$

for all admissible variations

$$\begin{aligned} \delta \theta &\in [H^1(B_0)], \quad \delta \theta = 0 \quad \text{on } \partial B_\theta, \\ \delta \bar{\lambda} &\in [H^{-\frac{1}{2}}(S_0)]. \end{aligned} \tag{27}$$

In Eq. (26), the normal heat flux,  $\mathbf{Q}^p \cdot \mathbf{N}$ , added to the body is obtained from (22). Eqs. (24) and (26) constitute a system of strongly coupled residual equations solved using a staggered scheme discussed in Section 4.3.

### 3.3. Propellant regression

A classical Galerkin weighted residual method is used to derive the variational formulation of (17). The variational statement reads: find  $\Phi^l \in L_2(\Omega_0)$ , such that

$$\int_{\Omega_0} \Phi^l w dV_0 = - \int_{\Omega_0} v_\epsilon w dV_0 \tag{28}$$

for all admissible variations  $w \in L_2(\Omega_0)$ .

## 4. Numerical implementation

In this section, we describe the numerical discretization and implementation of Eqs. (24), (26), and (28) within the context of the generalized finite element method. Let the domain  $B_0$  be divided into  $N^e$  elements  $B_0^e$ , with the element edges chosen independently of the interfaces  $S_0$  and  $\Gamma_1^0$ . Let the discretization be composed of  $N_j$  displacement and temperature nodes, with partition of unity shape functions  $\chi$  used to describe the geometry and the coordinates in the reference configuration  $B_0$ . Let  $\omega_j$  be the support of any node  $n_j^{u,\theta} \in N_j$ . A set of enriched nodes  $N_i$  (Fig. 4(a)) is then defined as

$$N_i = \{ n_j^{u,\theta} | n_j^{u,\theta} \in N_j, \omega_j \cap S_0 \neq \emptyset \}. \tag{29}$$

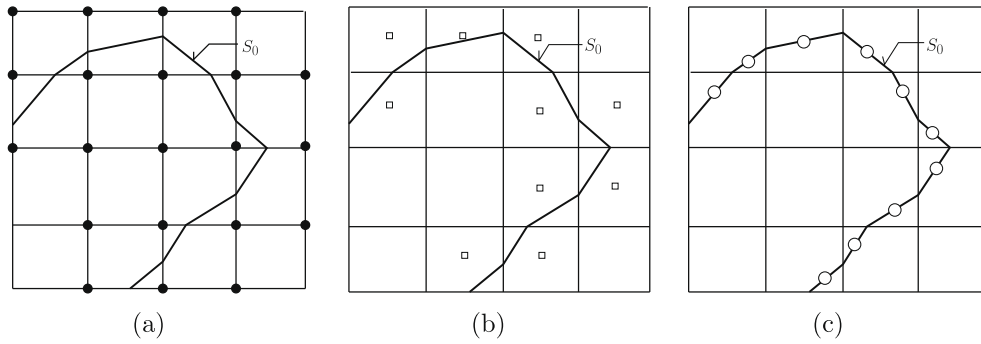


**Fig. 4.** Section of the finite element mesh in the vicinity of the material interface  $S_0$  showing (a) the enriched displacement nodes for a bilinear  $Q_1$  element; (b) the enriched pressure/volumetric nodes at element centers for a piecewise constant pressure/volume  $P_0$  element; and (c) the nodes for the Lagrange multiplier field.

The approximate displacement field  $\tilde{\mathbf{u}}$  is composed of a standard (*coarse*) displacement field  $\tilde{\mathbf{u}}^c$  and a set of  $\alpha$  enriched (*fine*) displacement fields  $\tilde{\mathbf{u}}_\alpha^e$  as

$$\tilde{\mathbf{u}}(\mathbf{X}) = \underbrace{\sum_j^{N_j} \chi_j(\mathbf{X}) \hat{\mathbf{u}}_j}_{\tilde{\mathbf{u}}^c(\mathbf{X})} + \sum_\alpha \underbrace{\sum_i^{N_i} \chi_i(\mathbf{X}) \psi^\alpha \hat{\mathbf{a}}_i^{\alpha^u}}_{\tilde{\mathbf{u}}_\alpha^e(\mathbf{X})}, \quad (30)$$

and a similar approximation for the temperature field  $\Theta$  yields

$$\tilde{\Theta}(\mathbf{X}) = \underbrace{\sum_j^{N_j} \chi_j(\mathbf{X}) \hat{\Theta}_j}_{\tilde{\Theta}^c(\mathbf{X})} + \sum_\alpha \underbrace{\sum_i^{N_i} \chi_i(\mathbf{X}) \psi^\alpha \hat{\mathbf{a}}_i^{\alpha^\Theta}}_{\tilde{\Theta}_\alpha^e(\mathbf{X})}, \quad (31)$$

where every node  $I \in N_i$  is enriched with  $\alpha$  linearly independent enrichment functions  $\psi^\alpha$  and  $(\hat{\mathbf{a}}_i^{\alpha^u}, \hat{\mathbf{a}}_i^{\alpha^\Theta})$  are the additional degrees of freedom introduced to approximate the *fine* enriched displacement and temperature  $(\tilde{\mathbf{u}}_\alpha^e, \tilde{\Theta}_\alpha^e)$  fields.

The approximations to pressure  $p$  and volumetric field  $\gamma$  are constructed from partition of unity shape functions as well. The pressure nodes  $N_j^p$  and the volumetric nodes  $N_j^\gamma$  are enriched if their supports  $\omega_j^p$  and  $\omega_j^\gamma$  are intersected by the interface  $S_0$ , as shown in Fig. 4(b):

$$\begin{aligned} N_i^p &= \{n_i^p | n_i^p \in N_j^p, \omega_j^p \cap S_0 \neq \emptyset\}, \\ N_i^\gamma &= \{n_i^\gamma | n_i^\gamma \in N_j^\gamma, \omega_j^\gamma \cap S_0 \neq \emptyset\}. \end{aligned} \quad (32)$$

As in (30), approximations of pressure  $\tilde{p}$  and volumetric field  $\tilde{\gamma}$  can be constructed as

$$\begin{aligned} \tilde{p}(\mathbf{X}) &= \underbrace{\sum_j^{N_j^p} \chi_j^p(\mathbf{X}) \hat{p}_j}_{\tilde{p}^c(\mathbf{X})} + \sum_{\alpha^p} \underbrace{\sum_i^{N_i^p} \chi_i^p(\mathbf{X}) \psi^{\alpha^p} \hat{\mathbf{a}}_i^{\alpha^p}}_{\tilde{p}_{\alpha^p}^e(\mathbf{X})}, \\ \tilde{\gamma}(\mathbf{X}) &= \underbrace{\sum_j^{N_j^\gamma} \chi_j^\gamma(\mathbf{X}) \hat{\gamma}_j}_{\tilde{\gamma}^c(\mathbf{X})} + \sum_{\alpha^\gamma} \underbrace{\sum_i^{N_i^\gamma} \chi_i^\gamma(\mathbf{X}) \psi^{\alpha^\gamma} \hat{\mathbf{a}}_i^{\alpha^\gamma}}_{\tilde{\gamma}_{\alpha^\gamma}^e(\mathbf{X})}. \end{aligned} \quad (33)$$

The Lagrange multiplier  $\lambda$ , introduced in (23), is discretized along the interface  $S_0$  and is illustrated in Fig. 4(c). A similar discretization is adopted for the Lagrange multiplier field  $\tilde{\lambda}$  in (26). The discretization enables construction of the approximate Lagrange multiplier fields,  $\tilde{\lambda}$  and  $\tilde{\tilde{\lambda}}$ , as

$$\begin{aligned} \tilde{\lambda}(\mathbf{X}) &= \sum_{j=1}^{N^\lambda} \chi_j^\lambda(\mathbf{X}) \hat{\lambda}_j, \\ \tilde{\tilde{\lambda}}(\mathbf{X}) &= \sum_{j=1}^{N^\lambda} \chi_j^\lambda(\mathbf{X}) \hat{\tilde{\lambda}}_j, \end{aligned} \quad (34)$$

where  $N^\lambda$  is the set of Lagrange multiplier nodes in the discretization. In the numerical examples presented in Section 5, we use  $Q_1/P_0/V_0$ ,  $Q_1$ , and piecewise constant finite elements for the mixed displacement–pressure–volume  $(\tilde{\mathbf{u}}, \tilde{p}, \tilde{\gamma})$ , temperature  $\tilde{\Theta}$ , and Lagrange multipliers  $(\tilde{\lambda}, \tilde{\tilde{\lambda}})$ , respectively.

Upon substituting the approximations for  $(\mathbf{u}, p, \gamma, \lambda)$  in (24), the following system of nonlinear Euler–Lagrange equations is obtained:

$$\begin{aligned}
 \mathcal{R}_{\mathbf{u}^s} &= \int_{B_0^\pm} \beta^2 \hat{\mathbf{P}} : \delta \bar{\mathbf{F}}^s dV_0 + \int_{B_0^\pm} \beta^3 \tilde{p} \bar{\mathbf{F}}^{-T} : \delta \bar{\mathbf{F}}^s dV_0 \\
 &\quad + \int_{S_0} \tilde{\lambda} \cdot \llbracket \delta \tilde{\mathbf{u}}^s \rrbracket dS_0 = 0, \\
 \mathcal{R}_{\mathbf{u}^e} &= \int_{B_0^\pm} \beta^2 \hat{\mathbf{P}} : \delta \bar{\mathbf{F}}_\alpha^e dV_0 + \int_{B_0^\pm} \beta^3 \tilde{p} \bar{\mathbf{F}}^{-T} : \delta \bar{\mathbf{F}}_\alpha^e dV_0 \\
 &\quad + \int_{S_0} \tilde{\lambda} \cdot \llbracket \delta \tilde{\mathbf{u}}_\alpha^e \rrbracket dS_0 = 0, \\
 \mathcal{R}_{p^s} &= \int_{B_0^\pm} (\tilde{J} - \tilde{\gamma} \beta^3) \delta \tilde{p}^s dV_0 = 0, \\
 \mathcal{R}_{p^e} &= \int_{B_0^\pm} (\tilde{J} - \tilde{\gamma} \beta^3) \delta \tilde{p}_{\alpha p}^e dV_0 = 0, \\
 \mathcal{R}_{\gamma^s} &= \int_{B_0^\pm} (\beta^3 U'(\tilde{\gamma}) - \tilde{p}) \delta \tilde{\gamma}^s dV_0 = 0, \\
 \mathcal{R}_{\gamma^e} &= \int_{B_0^\pm} (\beta^3 U'(\tilde{\gamma}) - \tilde{p}) \delta \tilde{\gamma}_{\alpha i}^e dV_0 = 0, \\
 \mathcal{R}_\lambda &= \int_{S_0} \delta \tilde{\lambda} \cdot \llbracket \tilde{\mathbf{u}}^s + \tilde{\mathbf{u}}_\alpha^e \rrbracket dS_0 = 0.
 \end{aligned} \tag{35}$$

An optimally (quadratically) convergent Newton–Raphson scheme is obtained through consistent linearization of the system of residual Eqs. (35), as detailed in [12].

The evolution of temperature  $\theta$  between  $[t_n, t_{n+1}]$  is tracked using a backward Euler algorithm with a time step size of  $\Delta t = t_{n+1} - t_n$  and the time derivative is evaluated using  $\dot{\theta} = (\theta^{n+1} - \theta^n)/\Delta t$ . Since we are not interested in ignition, early-time dynamics are not important, and thus, the backward Euler algorithm is acceptable. Residual equations are obtained by substituting the discrete form of temperature  $\theta$  (31) and  $\tilde{\lambda}$  in (15) and (26):

$$\begin{aligned}
 \mathcal{R}_\theta &= \int_{B_0^\pm} \delta \tilde{\theta} \rho_0 c \left\{ \frac{\tilde{\theta}^{n+1} - \tilde{\theta}^n}{\Delta t} \right\} dV_0 + \int_{B_0^\pm} \nabla_{\mathbf{x}} \delta \tilde{\theta} \cdot (-J^{n+1} \Lambda(\tilde{\theta}^{n+1})) \mathbf{C}^{-n+1} \nabla_{\mathbf{x}} \tilde{\theta}^{n+1} dV_0 \\
 &\quad + \int_{S_0} \tilde{\lambda} \llbracket \delta \tilde{\theta} \rrbracket dS_0 - \int_{\partial B_p} \delta \tilde{\theta} \mathbf{Q}^p \cdot \mathbf{N} dS_p = 0, \\
 \mathcal{R}_\lambda &= \int_{S_0} \delta \tilde{\lambda} \llbracket \tilde{\theta}^{n+1} \rrbracket dS_0 = 0.
 \end{aligned} \tag{36}$$

Here again, we employ the Newton–Raphson method to solve the system of nonlinear Eqs. (36) and consistent linearization of (36) is given in Appendix A.

#### 4.1. Geometry description and numerical integration

In this work, we describe the interfaces  $S_0$  and  $I_1^0$  as zero level sets of scalar functions  $\Phi(\mathbf{X})$  and  $\Phi^I(\mathbf{X})$ , respectively. The scalar level set functions are then approximated using the standard basis function  $\chi$  as

$$\Phi(\mathbf{X}) = \sum_{N_j} \chi_j \hat{\Phi}(\mathbf{X}_j), \tag{37}$$

and

$$\Phi^I(\mathbf{X}) = \sum_{N_j} \chi_j \hat{\Phi}^I(\mathbf{X}_j). \tag{38}$$

In the above equation, the nodal level set function  $\hat{\Phi}$  is constructed at every node  $J$  as

$$\hat{\Phi}(\mathbf{X}_j) = \text{sign}((\mathbf{X}_j - \mathbf{X}_i) \cdot \mathbf{N}) \min(\|\mathbf{X}_j - \mathbf{X}_i\|), \tag{39}$$

where  $\mathbf{X}_i$  denotes any point on the interface  $S_0$  and  $\mathbf{N}$  is the outward pointing normal at  $\mathbf{X}_i$ . As a result, each node in the finite element mesh stores an additional scalar  $\hat{\Phi}$ , which is then used to track/detect the existence of an interface. A similar approach is adopted to construct the level set scalar function  $\hat{\Phi}^I$ . In the present study, the material interface  $S_0$  is stationary, and hence the level set function  $\Phi(\mathbf{X})$  is computed at the outset and remains unchanged thereafter. For each node, the sign of the level set function  $\Phi$  is used to check its position in  $B_0^+, B_0^-$  or on  $S_0$ , and elements are assigned to  $B_0^+, B_0^-$  or an intersected

element set that contain a interface  $S_0$ . Similarly, the sign of the level set function  $\Phi^l$  is used to check if a point lies inside the fluid or solid domain. Implementation details on the detection of the interface can be found in [25].

Conventional Gaussian quadrature is used to integrate the volume integrals in elements that lie completely in  $B_0^+$  or  $B_0^-$  and the integrals in elements intersected by an interface are computed on partitioned sub-triangles [11].

#### 4.2. Propellant regression

The temporal and spatial discretization of (28) is similar to that adopted by Mourad et al. [18], where an explicit first-order Euler method is used to integrate the system of ODEs that describe the level set function  $\Phi^l$  at each node  $i$ . The ODEs are then decoupled by using a lumped mass matrix strategy and the resulting nodal update is given by

$$\Phi_i^{l,n+1} = \Phi_i^{l,n} - \Delta t (v_e)_i^n. \quad (40)$$

The CFL condition that accompanies (40) is

$$\max_{i \in N_l} (v_e)_i \Delta t \leq h. \quad (41)$$

In the simulations performed in this study, the time step  $\Delta t$  required to obtain temporally accurate solutions for the temperature field (36) is smaller than the CFL condition (41), which is therefore automatically satisfied. The propellant surface is discretized as a set of piecewise linear segments and we adopt the strategy described in Mourad et al. [18] to construct the extension velocity field from the surface regression rates  $r_b$ . The extension velocity  $v_e$  at any node  $i$  is evaluated as

$$(v_e)_i = v_e|_{\Gamma_i^0}, \quad (42)$$

such that  $\|\mathbf{X}_{i^0} - \mathbf{X}_i\|$  is minimum for all points on  $\Gamma_i^0$ . Note that for a heterogeneous solid propellant, the propellant surface regression rate is discontinuous at material interfaces, and consequently the extension velocities  $v_e$  constructed from the surface regression rates are also discontinuous. However, observations by Mourad et al. [18] suggest that the discontinuity in the extension velocity field do not lead to unstable or oscillatory solutions.

#### 4.3. Operator split methodology

To partition the coupled system (35) and (36) for efficient numerical implementation, a two-stage staggered scheme based on the isothermal split is used. In the first stage, the mechanical phase (9) is solved with the fixed temperature (isothermal phase), and, in the second stage, the thermal phase (16) is solved during which the configuration or shape of the body is held fixed. To summarize, the governing equations solved during the two stages are

##### 1. Mechanical phase:

$$\begin{aligned} \nabla_{\mathbf{x}} \cdot \mathbf{P} &= \mathbf{0}, \\ \dot{\Theta} &= 0. \end{aligned} \quad (43)$$

##### 2. Thermal phase:

$$\begin{aligned} \dot{\Phi} &= \mathbf{0}, \\ \rho_0 c \dot{\Theta} - \nabla_{\mathbf{x}} \cdot \mathbf{Q} &= 0. \end{aligned} \quad (44)$$

The solution to the coupled problem is then attained iteratively using an algorithm similar to the one proposed by Ji et al. [17]. Let  $(\cdot)^{n,k}$  denote values at time level  $n$  and iteration level  $k$ , while  $(\cdot)^n$  and  $(\cdot)^{n+1}$  denote converged values at time levels  $n$  and  $n+1$ . The iterations are stopped upon satisfaction of the convergence criteria defined below:

$$S_u = \frac{\|\tilde{\mathbf{u}}^{n+1,k+1} - \tilde{\mathbf{u}}^{n+1,k}\|_2}{\|\tilde{\mathbf{u}}^{n+1,0}\|_2} \leq S_{\text{tol}}^u \quad (45)$$

and

$$S_\theta = \frac{\|\tilde{\Theta}^{n+1,k+1} - \tilde{\Theta}^{n+1,k}\|_2}{\|\tilde{\Theta}^{n+1,0}\|_2} \leq S_{\text{tol}}^\theta. \quad (46)$$

The tolerances  $S_{\text{tol}}^u$  and  $S_{\text{tol}}^\theta$  are chosen to be 1e-05 for the numerical examples presented below. Details on the algorithm associated with the operator split method are provided in Appendix B.

### 5. Numerical examples

In this section, convergence tests are carried out to assess the performance of the numerical methodologies developed in Section 3. Furthermore, to ascertain the robustness of the numerical method, the regression of sandwich and heterogeneous

solid propellants is simulated. As mentioned before, the finite elements considered for the studies are the classical  $Q_1/P_0/V_0$  elements for the displacements and the bilinear element for temperature. The *Heaviside* function [12] is used as an enrichment for the pressure and volume fields in (33). A low-order, piecewise constant approximation for the Lagrange multiplier is adopted as well. For simulations of regression of the solid propellant, portions of the finite elements lying in the fluid phase  $\Omega'_0$  are omitted from volumetric integrations, akin to the treatment of holes described in [25].

### 5.1. Convergence tests

We turn our attention to a spatial mesh convergence study of the non-standard GFEM-based thermomechanical solver discussed in Section 4. The spatial convergence is assessed by assuming steady-state conditions, i.e., neglecting the time derivative of temperature  $\Theta$  in (16), and a non-regressing propellant surface is considered. The study is performed on a square propellant domain of length  $L = 2$  mm (the *matrix*) filled with a circular inclusion (the *particle*) of radius  $a = 0.4$  mm (Fig. 5(a)) and is carried out using  $Q_1/P_0/V_0$  elements under 2-D plane strain conditions. The thermomechanical properties of individual constituents are listed in Table 1. The AP particles are modeled as a compressible solid whereas the binder is a nearly-incompressible one. The bottom surface of the propellant is restrained in the  $y$  direction and has a fixed temperature of 300 K. To remove rigid-body modes, point  $P$  is restrained in the  $x$  direction. A constant normal heat flux of  $75.31 \text{ J/m}^2 (= 18 \text{ cal/m}^2)$ , which is applied on the propellant top surface and is kept traction-free, while adiabatic wall conditions are imposed on the other two sides with traction-free boundaries as well. A level set function (39) is used to describe the circular inclusion, where the level set function is positive outside the circular inclusion and negative inside. The convergence study is carried out on structured uniform grids composed of  $10 \times 10$ ,  $20 \times 20$ ,  $40 \times 40$  and  $80 \times 80$  elements. These discretizations provide an element size  $h$  of 200, 100, 50 and 25  $\mu\text{m}$ , respectively. A typical mesh for the convergence study is shown in Fig. 5(b).

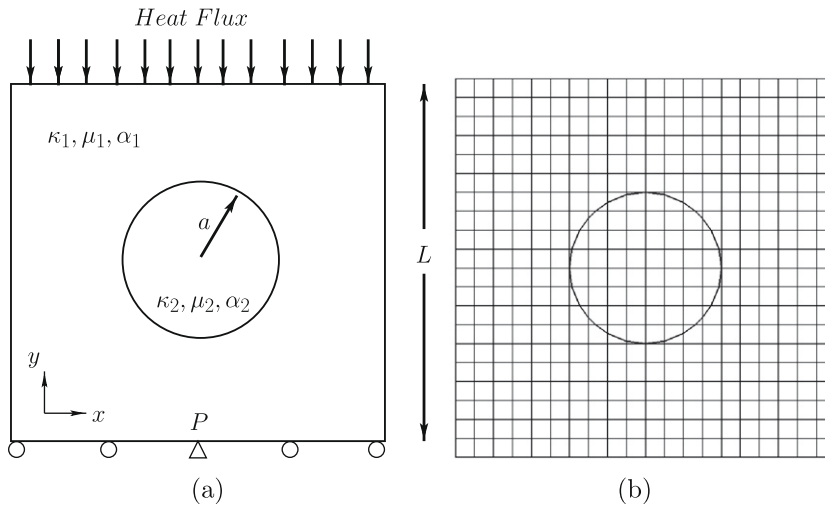


Fig. 5. (a) Schematic of the boundary value problem used for mesh convergence tests; (b) a sample  $20 \times 20$  finite element mesh.

Table 1

Material properties of constituents of the heterogeneous solid propellant. Values superscripted by  $a$  are taken from [26] and values superscripted by  $b$  are taken from [14]. A range of values for the coefficient of linear expansion is found in literature and typical values are chosen here.

Property	Symbol	AP	Binder
Bulk modulus <sup>a</sup> (MPa)	$\kappa$	14,950	12,500
Shear modulus <sup>a</sup> (MPa)	$\mu$	10,670	2.5
Coefft. of linear expansion ( $\text{K}^{-1}$ )	$\tilde{\alpha}$	$1e-05$	$1e-04$
Thermal conductivity <sup>b</sup> ( $\text{Wm}^{-1} \text{K}^{-1}$ )	$\lambda$	0.405	0.276
Density <sup>b</sup> ( $\text{kg m}^{-3}$ )	$\rho$	1920	950
Specific heat <sup>b</sup> ( $\text{J kg}^{-1} \text{K}^{-1}$ )	$c$	1255.2	1255.2
Activation energy <sup>b</sup> (K)	$E_a/R$	11,000	7500
Arrhenius constant <sup>b</sup> ( $\text{m s}^{-1}$ )	$A$	1450	10.36
Heat of reaction <sup>b</sup> ( $\text{J kg}^{-1}$ )	$q^s$	-418,400	-196,648

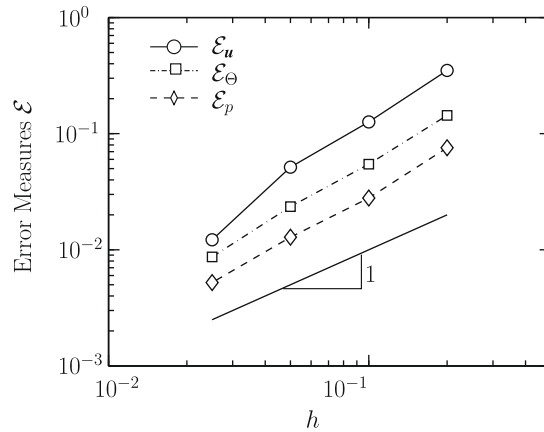


Fig. 6. Errors in displacement  $\mathcal{E}_u$ , temperature  $\mathcal{E}_\theta$  and pressure  $\mathcal{E}_p$  as a function of varying mesh size  $h$  (mm) plotted on a logarithmic scale.

The errors in displacement and temperature,  $\mathcal{E}_u$  and  $\mathcal{E}_\theta$ , are defined using typical  $H^1$  Sobolev norms

$$\begin{aligned}\mathcal{E}_u &= \|\tilde{\mathbf{u}} - \mathbf{u}_{\text{ref}}\|_{H^1} = \sqrt{\|\tilde{\mathbf{u}} - \mathbf{u}_{\text{ref}}\|^2 + \|\nabla \tilde{\mathbf{u}} - \nabla \mathbf{u}_{\text{ref}}\|^2}, \\ \mathcal{E}_\theta &= \|\tilde{\theta} - \theta_{\text{ref}}\|_{H^1} = \sqrt{\|\tilde{\theta} - \theta_{\text{ref}}\|^2 + \|\nabla \tilde{\theta} - \nabla \theta_{\text{ref}}\|^2},\end{aligned}\quad (47)$$

while the error measure  $\mathcal{E}_p$  for the pressure field is defined as

$$\mathcal{E}_p = \|\tilde{p} - p_{\text{ref}}\|_{L_2}. \quad (48)$$

Due to the absence of an analytical solution for the nonlinear problem discussed here, a *fine* finite element mesh composed of 42,636  $Q_1/P_0/V_0$  elements and 43,037 nodes, that conforms to the bimaterial interface, is used as the reference solution in (47) and (48). Fig. 6 reports the results for the convergence tests in terms of the dependence of the errors  $\mathcal{E}_u$ ,  $\mathcal{E}_\theta$  and  $\mathcal{E}_p$  on the mesh size  $h$ . It is observed that the convergence rates for the numerical method described in Section 4 are in correspondence with the optimal convergence rate of one.

## 5.2. Regression of a sandwich propellant

To assess the spatial accuracy of the coupled thermomechanical solver with propellant surface regression, a problem with a steady-state solution is highly desired. For this purpose, a sandwich propellant that consists of a two-dimensional periodic array of alternating AP and binder slices in stoichiometric proportions is often used [19]. We start this study by neglecting the deformation (rigid sandwich propellant) to investigate the spatial convergence of the thermal solver. We then include the thermomechanical deformations to study their effect on the computed regression rates.

The periodic length of the sandwich propellant is 0.24 mm with the binder filling the middle 0.04-wide region and the remainder consisting of AP, as shown in Fig. 7. The material properties of AP and binder are those listed earlier in Table 1 and the sandwich propellant surface is subjected to a constant heat flux  $Q^f$  of  $836.8 \text{ J/m}^2 (= 200 \text{ cal/m}^2)$ . The problem is symmetric about the center line, and thus, only half of the domain is simulated.

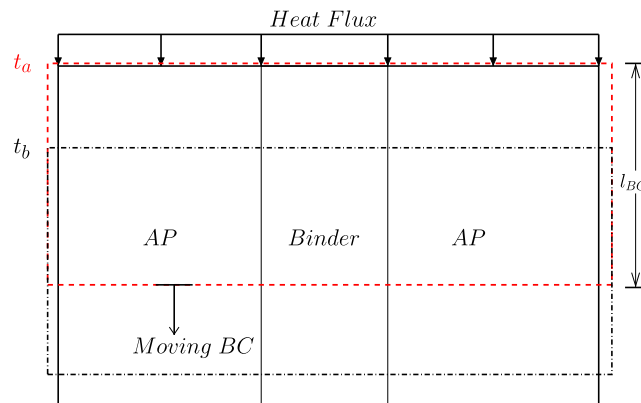


Fig. 7. Schematic of sandwich propellant showing the moving window at times  $t_a$  and  $t_b$ .

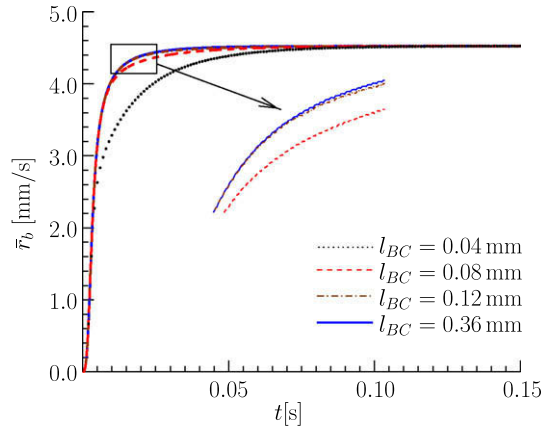


Fig. 8. Evolution of propellant surface average regression rate for varying window sizes  $l_{BC}$ .

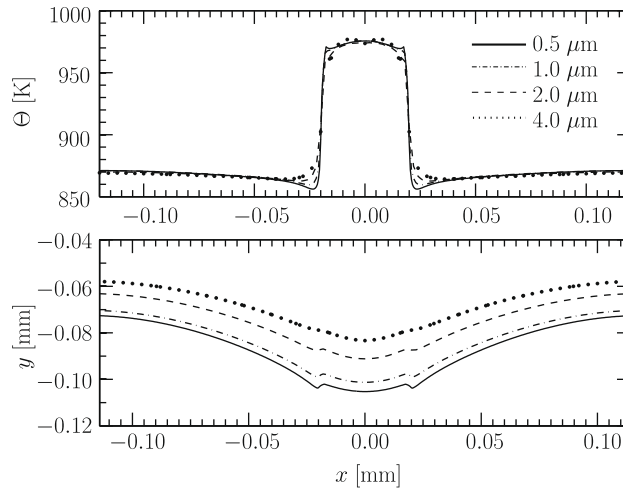


Fig. 9. Spatial convergence of surface temperature profiles and surface positions for the rigid sandwich propellant for different grid sizes.

To enable faster computations, only the portion of the sandwich propellant enclosed within a moving window is considered. The lower-edge boundary conditions are imposed on the lower end of the window and the length of the window  $l_{BC}$  is varied to determine the effect of window size on the resulting regression rates  $\bar{r}_b$ , defined by

$$\bar{r}_b(t) = \frac{\int_{r_1^0} r_b(s, t) ds}{\int_{r_1^0} ds}, \tag{49}$$

where  $s$  is the parametric coordinate along the propellant surface  $\Gamma_1^0$ . Four window sizes of 0.04, 0.08, 0.12 and 0.36 mm are chosen for this experiment and the results are depicted in Fig. 8. It is observed from Fig. 8 that a window size of 0.12 mm is sufficient to capture the transient solutions and is therefore used in all simulations reported hereafter.

The regression of the rigid sandwich propellant is studied on four different meshes of sizes 0.5, 1.0, 2.0 and 4.0  $\mu\text{m}$ , respectively. Fig. 9 shows the spatial distribution of the steady-state surface temperatures and the position of the propellant surface after  $t = 0.15$  s, with a temporally converged time step of  $\Delta t = 2.5 \times 10^{-5}$  s. The surface temperature and position profiles demonstrate spatial convergence of the method and also enable choice of a suitable grid size  $h$  for similar simulations. The time evolution of the average regression rate  $\bar{r}_b$  (49) is shown in Fig. 10 and a closer examination of the steady-state average regression rate evolution profile reveals periodic oscillations with amplitudes that are dependent on grid size  $h$ . Furthermore, the amplitude of these oscillations decreases with grid size  $h$ , also observed by Wang et al. [14].

In addition to the spatially averaged regression rates  $\bar{r}_b$  defined in (49), we study the effect of the mesh size on the time-average regression rate  $\bar{\bar{r}}_b$  computed in a steady-state time interval  $[t_1, t_2]$  defined by

$$\bar{\bar{r}}_b = \frac{\int_{t_1}^{t_2} \bar{r}_b(t) dt}{(t_2 - t_1)}. \tag{50}$$

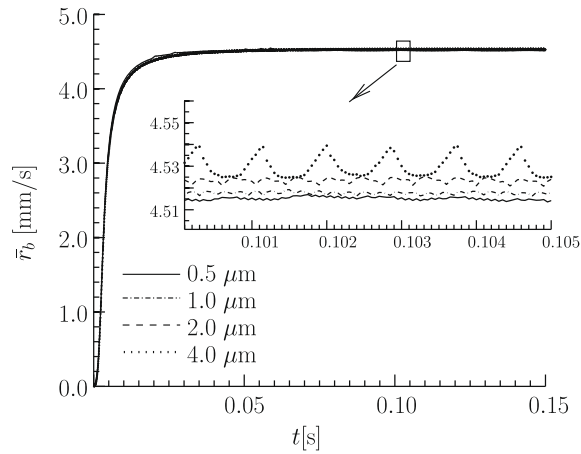


**Fig. 10.** Evolution of average regression rate  $\bar{r}_b$  for different mesh sizes. Inset shows a magnified portion of the plot in the time interval [0.100,0.105]s.

The absolute error  $\mathcal{E}_I = \text{abs}(\bar{r}_b - \bar{r}_b^{\text{fine}}) / \bar{r}_b^{\text{fine}}$  is evaluated with respect to the finest grid (0.5  $\mu\text{m}$ ) and the overall order is  $\mathcal{O}_I = \ln(\mathcal{E}_I^{2h} / \mathcal{E}_I^h) / \ln(2)$ . The results are reported in Table 2. It is observed that the overall convergence rate of the time-average regression rate is approximately 0.91, consistent with the first-order backward Euler time stepping algorithm used here.

We now consider the regression of a deformable sandwich propellant that expands under the influence of large thermal gradients in the vicinity of the propellant surface. A grid size of 1  $\mu\text{m}$ , based on results tabulated in Table 2, and a time step of  $\Delta t = 2.5 \times 10^{-5}$  s are chosen for this simulation. The spatial distributions of the temperature and equivalent strains within the sandwich propellant are shown in Fig. 11. The thermal gradients decrease rapidly away from the propellant surface and a large portion of the thermomechanical strains are found within the thermal boundary layer. In particular, large thermomechanical strains concentrate in binder regions close to the AP/Binder material interfaces. These large strains are attributed to large thermal gradients as well as the highly disparate material properties of AP and the binder (Table 1). The binder experiences large strains approaching 45% which justifies the use of large deformation kinematics for such heterogeneous solid

**Table 2**

Time-average regression rate  $\bar{r}_b$  as a function of grid size  $h$  computed in the time interval [0.10,0.15]s. The absolute error  $\mathcal{E}_I$  and the total order  $\mathcal{O}_I$  of the numerical scheme are also listed.

$h$ ( $\mu\text{m}$ )	$\bar{r}_b$ (mm/s)	$\mathcal{E}_I$	$\mathcal{O}_I$
0.5	4.5118		
1.0	4.5183	0.0064	
2.0	4.5239	0.0121	0.9072
4.0	4.5315	0.0197	0.7017

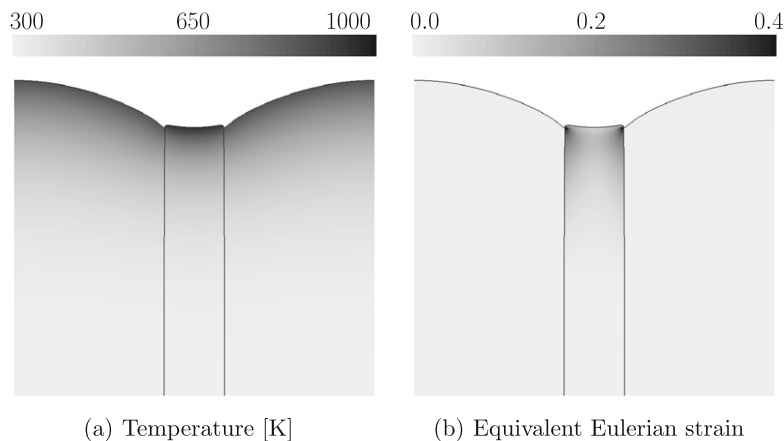


**Fig. 11.** Steady-state spatial distribution of (a) temperature and (b) equivalent strains.

propellant systems. Furthermore, it is observed that most of the thermal strain energy is stored in the binder while the kinematic response of AP is rigid-like (due to its high stiffness).

Fig. 12 compares the steady-state regression rates  $\bar{r}_b$  between a rigid and a deformable sandwich propellant. The steady-state regression rate of the deformable sandwich propellant is found to be lower than the rigid sandwich propellant for identical material properties and grid sizes. Similar observations were reported by Kuznetsov and Stewart [7], albeit for one-dimensional homogeneous solid propellants. The aforementioned oscillations in the regression rate are larger for the deformable sandwich propellant than for its rigid counterpart.

In addition to the regression rates, differences are also observed in the surface temperature and shape profiles as shown in Fig. 13. In regions farther from the AP/binder interface, the surface temperature profiles are similar and attain steady-state temperatures of 872 K at  $x = \pm 0.12$  and 974 K at  $x = 0$ , while the deformable sandwich propellant has lower surface temperatures in the vicinity of the AP/binder interface ( $x \in [-0.02, 0.02]$ ). Fig. 13 also presents the shape of the propellant surface. The surface shape, overlaid such that the two shapes coincide at  $x = 0$ , shows significant differences in the surface curvature due to the large thermal expansions at the propellant surface. The large extent of thermal expansion in the binder is also evident in Fig. 14, where the magnitude of the displacements  $\|\mathbf{u}\|$  is plotted along the propellant surface.

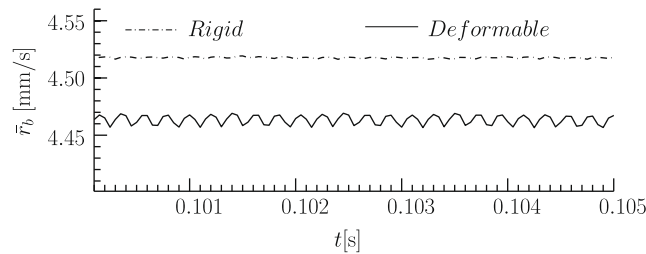


Fig. 12. Comparison of steady-state average regression rate  $\bar{r}_b$  for rigid and deformable sandwich propellant.

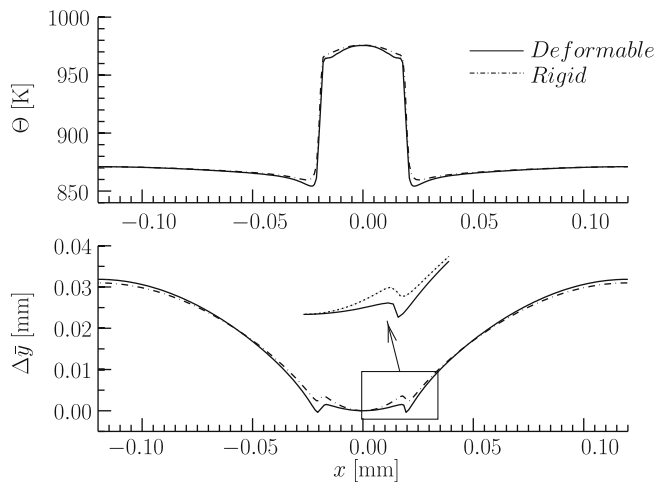


Fig. 13. Comparison of steady-state surface temperature and deformed shape for rigid and deformable sandwich propellant. For ease of comparison, the surface shapes are overlaid so as to coincide at  $x = 0$ .

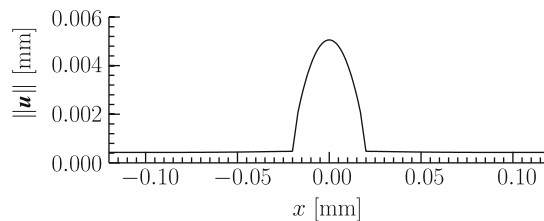


Fig. 14. Magnitude of displacement  $\|\mathbf{u}\|$  along the surface of the sandwich propellant.

### 5.3. Regression of a heterogeneous propellant

We now examine the effects of coupled thermomechanical processes on the regression rate of a two-dimensional heterogeneous solid propellant pack. As described in Section 5.2, the heterogeneous solid propellant is composed of very stiff but compressible Ammonium Perchlorate (AP) particles of various sizes embedded in a much more compliant quasi-incompressible binder. The pack is constructed by stacking periodic square-shaped packs one above the other and in this example three square-shaped packs of size 0.12 mm are used as shown in Fig. 15. The material properties are again listed in Table 1. A heat flux  $Q'$  of  $836.8 \text{ J/m}^2 (= 200 \text{ cal/m}^2)$  and a uniform pressure loading of 2 MPa, exerted by the fluid phase on the solid propellant surface, are applied on the propellant surface, while the sides of the pack are periodic. A moving window, described in Section 5.2, of length  $l_{BC} = 0.12 \text{ mm}$  is used to reduce the computational effort and the displacement degrees of freedom at the bottom surface of the moving window are free to move horizontally but restrained vertically, while the temperature at the bottom surface of the moving window is held fixed at 300 K. Here again, we adopt a structured finite element mesh independent of the circular particles and the regressing propellant surface,  $h = 1 \mu\text{m}$  (Fig. 15).

Fig. 16 shows snapshots of the temperature and equivalent strain distributions in the heterogeneous propellant pack at times  $t = 0.01 \text{ s}$  and  $t = 0.05 \text{ s}$ . Similar to the sandwich propellant (Fig. 11(a)), large thermal gradients are observed in the vicinity of the propellant surface for the heterogeneous propellant pack (Fig. 16(a)) and these gradients become negligible farther away from the propellant surface. The distribution of equivalent strain also shows large strains in the thermal boundary layer and rapidly decaying deformations away from propellant surface (Fig. 16(b)). Strains of 20–25% are present in the binder, considerably lower than those observed for the sandwich propellant, although similar thermal gradients exist. This fact is attributed to the different boundary conditions and smooth circular AP/Binder interface shapes. Furthermore, the highly strained regions of the binder are found between closely packed AP particles, suggesting strong inter-particle interactions.

As shown in Fig. 17, the instantaneous surface temperature profile shows large variations along the propellant surface. Sharp changes in the temperature profile occur in the vicinity of AP/Binder interfaces, with the binder exhibiting higher surface temperatures, while the temperature distribution is fairly homogeneous inside large AP particles.

A comparison of the evolution of the computed average regression rates  $\bar{r}_b$  for a rigid and deformable heterogeneous solid propellant pack is shown in Fig. 18. After the initial transients the evolution of the regression rate is periodic where each period represents regression of one square-shaped periodic pack shown in Fig. 15. Inset in Fig. 18 shows a portion of the regression rate evolution that contains a complete period of evolution. The time-average regression rates  $\bar{r}_b$  for the rigid and deformable propellant pack are then computed from the time required to regress one square-shaped pack. In Fig. 18, points  $A_R$  and  $B_R$  mark the end points of one complete period of rigid propellant regression, i.e., the time taken to regress one square-shaped pack, while points  $A_D$  and  $B_D$  mark the same for the deformable propellant pack. Similar to the sandwich propellant (Fig. 12), the computed time-average regression rate  $\bar{r}_b$  of the deformable solid propellant is lower than for its rigid counterpart by approximately 5.8%. Regression rates and their statistical variations are reported in Table 3. Standard

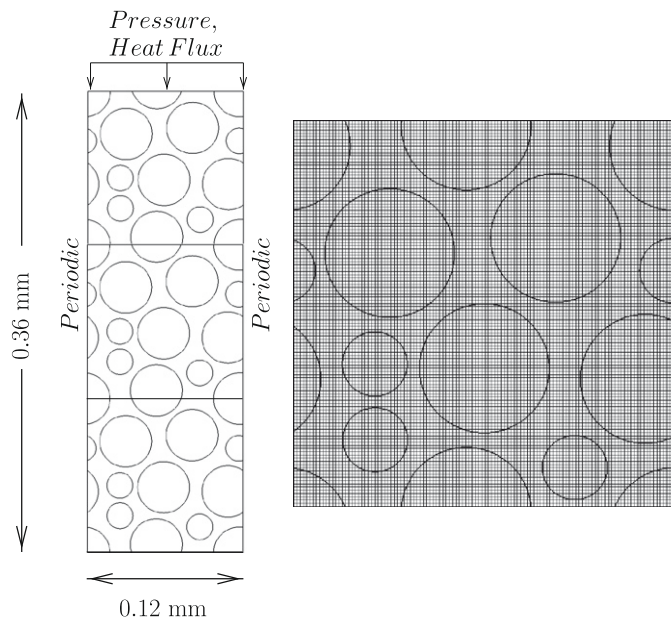
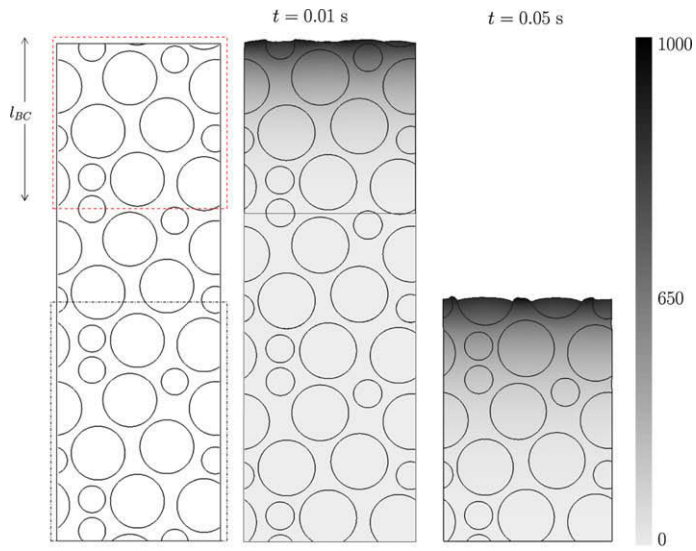
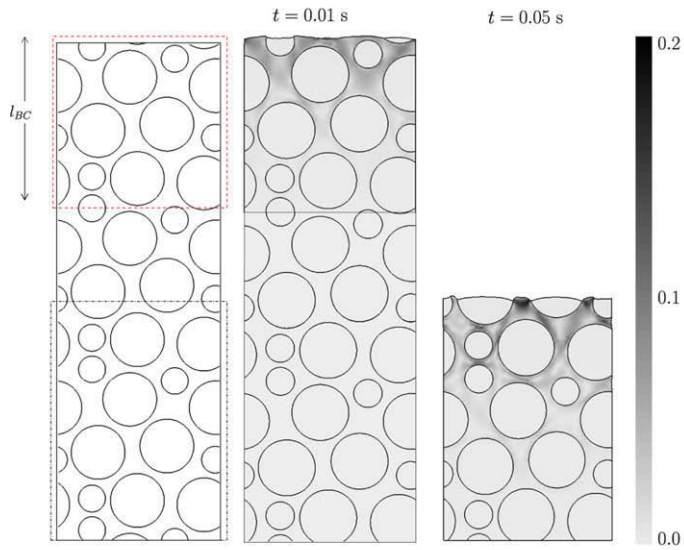


Fig. 15. Schematic of heterogeneous propellant pack with applied boundary conditions. A periodic pack with a  $1 \mu\text{m}$  mesh is shown beside the pack.



(a) Temperature [K]



(b) Equivalent Eulerian Strains

**Fig. 16.** Snapshots of heterogeneous solid propellant pack, taken at times  $t = 0.01$  s and  $t = 0.05$  s, showing spatial distribution of (a) temperature; (b) equivalent strains. The moving window at  $t = 0.01$  s is depicted by a red box and at  $t = 0.05$  s is depicted by a black box.

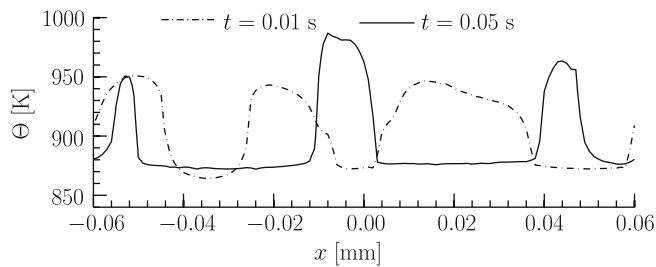


**Fig. 17.** Surface temperature profile of the heterogeneous propellant pack at times  $t = 0.01$  s and  $t = 0.05$  s.

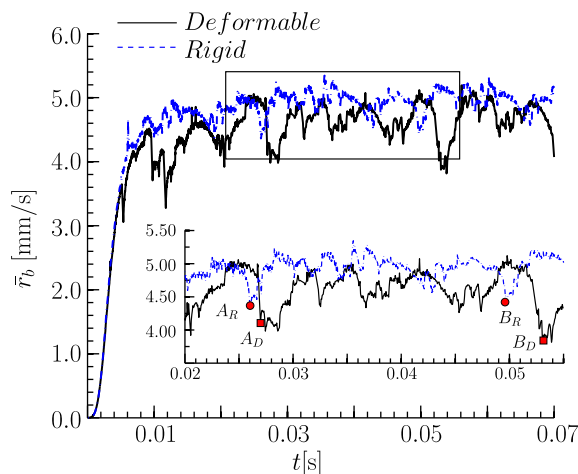


**Fig. 18.** Evolution of average regression rate  $\bar{r}_b$  with time  $t$  for rigid and deformable propellant packs. Inset shows a magnified portion of the plot that contains one complete period of evolution tagged by points  $(A_R, B_R)$  and  $(A_D, B_D)$ .

**Table 3**

Time-average regression rate  $\bar{\bar{r}}_b$  and the maximum and minimum values of the average regression rate  $\bar{r}_b$  for rigid and deformable propellant packs.

Propellant pack	$\bar{\bar{r}}_b$ (mm/s)	max $\bar{r}_b$ (mm/s)	min $\bar{r}_b$ (mm/s)	Standard deviation
Rigid	4.934	5.318	4.410	0.1560
Deformable	4.646	5.120	3.815	0.2595

deviations of the average regression rate  $\bar{r}_b$  indicate larger variations of instantaneous regression rates for the deformable solid propellant.

## 6. Conclusions

This manuscript has described a numerical framework that combines the generalized mixed finite element method with the assumed gradient level set method to model regression of thermomechanically deforming heterogeneous solid propellants. Spatial convergence of the coupled thermomechanical solver was numerically assessed and found to be optimal. Spatial convergence of the thermomechanical solver with surface regression was also assessed using a periodic sandwich propellant with the average regression rate used to quantify error measures. The scheme was found to have an overall order,  $\mathcal{O}_l$ , close to an optimal rate while employing a first-order backward Euler method. Finally, the regression of an idealized two-dimensional heterogeneous solid propellant pack was chosen to demonstrate the capability and robustness of the developed framework. It was found that the deformable heterogeneous propellant pack had smaller regression rates than the rigid one. It was also observed that, within the thermal boundary layer, the binder regions close to AP/binder interfaces experienced large thermomechanical strains.

## Acknowledgments

This work was supported by the Center for Simulation of Advanced Rockets (CSAR) under Contract Number B523819 by the US Department of Energy. K. Matouš also acknowledges support from ATK/Thiokol, ATK-21316 (J. Thompson and Dr. I.L. Davis – Program managers).

## Appendix A. Consistent linearization

A Newton–Raphson algorithm is used to solve the nonlinear system of equations (36). For simplicity, we assume the thermal conductivity  $\lambda$  to be a constant. Consistent linearization of (36) then yields

$$\begin{aligned}
 D\mathcal{R}[\delta\tilde{\Theta}, \Delta\tilde{\Theta}] &= \int_{B_0^\pm} \frac{\rho_0 c}{\Delta t} \delta\tilde{\Theta} \Delta\tilde{\Theta} dV_0 + \int_{B_0^\pm} (-JA) \nabla_X \delta\tilde{\Theta} \cdot \mathbf{C}^{-1} \nabla_X \Delta\tilde{\Theta} dV_0 - \int_{\partial B_p} \delta\tilde{\Theta} \frac{\partial(\mathbf{Q}^p, \mathbf{N})}{\partial\tilde{\Theta}} \Delta\tilde{\Theta} dS_p, \\
 D\mathcal{R}[\delta\tilde{\Theta}, \Delta\tilde{\lambda}] &= \int_{S_0} [\delta\tilde{\Theta}] \Delta\tilde{\lambda} dS_0, \\
 D\mathcal{R}[\delta\tilde{\lambda}, \Delta\tilde{\Theta}] &= \int_{S_0} \delta\tilde{\lambda} [\Delta\tilde{\Theta}] dS_0, \\
 D\mathcal{R}[\delta\tilde{\lambda}, \Delta\tilde{\lambda}] &= 0.
 \end{aligned} \tag{A.1}$$

## Appendix B. Algorithm for operator split

The algorithm adopted for the operator split methodology described in Section 4.3 is described below. Let  $(\cdot)^{n,k}$  denote values at time level  $n$  and iteration level  $k$ , while  $(\cdot)^n$  and  $(\cdot)^{n+1}$  denote converged values at time levels  $n$  and  $n+1$ .

1. Increment time  $t_n$  by  $\Delta t$ , i.e., set  $t_{n+1} = t_n + \Delta t$ . At  $t_{n+1}$ , evolve propellant surface through (40).
2. Set  $k = 0$  and  $(\cdot)^{n+1,0} = (\cdot)^n$  and compute
  - [(a)] If  $k = 0$ , set  $\tilde{\Theta}^{n+1,0} = \tilde{\Theta}^n$  and compute  $\tilde{\mathbf{u}}^{n+1,k+1}$  from (35) using  $\tilde{\Theta}^{n+1,k}$ .  
Compute  $\tilde{\Theta}^{n+1,k+1}$  from (36) using  $\tilde{\mathbf{u}}^{n+1,k+1}$ .
  - [(b)] Compute convergence criteria measures  $S_u$  and  $S_\Theta$  from (45) and (46).
  - [(c)] if  $S_u < S_{tol}^u$  and  $S_u < S_{tol}^\Theta$  then  
compute  $\nu_e^{n+1}$  from (42)  
Proceed to step 3.  
else  
set  $k = k + 1$  and goto step (a).  
end if
3. Return to step 1.

## References

- [1] B. Collins, F. Maggi, K. Matouš, T. Jackson, J. Buckmaster, Using tomography to characterize heterogeneous solid propellants, In: 46th AIAA Aerospace Sciences Meeting and Exhibit, 7–10 January, Reno, Nevada, Number 2008-0941, 2008.
- [2] S. Kochevets, J. Buckmaster, T.L. Jackson, A. Hegab, Random propellant packs and the flames they support, *Journal of Propulsion and Power* 17 (4) (2001) 883–891.
- [3] H.L. Berghout, S.F. Son, C.B. Skidmore, D.J. Idar, B.W. Asay, Combustion of damaged PBX 9501 explosive, *Thermochemica Acta* 384 (1–2) (2002) 261–277.
- [4] M. Kumar, K.K. Kuo, Effect of deformation on flame spreading and combustion in propellant cracks, *AIAA Journal* 19 (12) (1981) 1580–1589.
- [5] M. Kumar, S.M. Kovacic, K.K. Kuo, Flame propagation and combustion processes in solid propellant cracks, *AIAA Journal* 19 (5) (1981) 610–619.
- [6] K.K. Kuo, J. Moreci, J. Mantzaras, Different modes of crack propagation in burning solid propellants, *Journal of Propulsion and Power* 3 (1) (1987) 19–25.
- [7] I.R. Kuznetsov, D.S. Stewart, Burning rate of homogeneous energetic materials with thermal expansion and varying thermal properties in the condensed phase, *Combustion Theory and Modelling* 9 (2) (2005) 255–272.
- [8] C.A. Duarte, I. Babuška, J.T. Oden, Generalized finite element methods for three-dimensional structural mechanics problems, *Computers and Structures* 77 (2) (2000) 215–232.
- [9] T. Strouboulis, K. Copps, I. Babuška, The generalized finite element method, *Computer Methods in Applied Mechanics Engineering* 190 (32–33) (2001) 4081–4193.
- [10] T. Belytschko, T. Black, Elastic crack growth in finite elements with minimal remeshing, *International Journal for Numerical Methods in Engineering* 45 (5) (1999) 601–620.
- [11] N. Moës, J. Dolbow, T. Belytschko, A finite element method for crack growth without remeshing, *International Journal for Numerical Methods in Engineering* 46 (1) (1999) 131–150.
- [12] K.R. Srinivasan, K. Matouš, P.H. Geubelle, Generalized finite element method for modeling nearly incompressible bimaterial hyperelastic solids, *Computer Methods in Applied Mechanics Engineering* 197 (2008) 4882–4893.
- [13] S. Osher, J.A. Sethian, Fronts propagating with curvature-dependent speed – algorithms based on Hamilton–Jacobi formulations, *Journal of Computational Physics* 79 (1) (1988) 12–49.
- [14] X. Wang, T.L. Jackson, L. Massa, Numerical simulation of heterogeneous propellant combustion by a level set method, *Combustion Theory and Modelling* 8 (2) (2004) 227–254.
- [15] X. Wang, T.L. Jackson, The numerical simulation of two-dimensional aluminized composite solid propellant combustion, *Combustion Theory and Modelling* 9 (2005) 171–197.
- [16] X. Wang, K. Hossain, T.L. Jackson, The three-dimensional numerical simulation of aluminized composite solid propellant combustion, *Combustion Theory and Modelling* 12 (1) (2007) 45–71.
- [17] H. Ji, H. Mourad, E. Fried, J. Dolbow, Kinetics of thermally induced swelling of hydrogels, *International Journal of Solids and Structures* 43 (7–8) (2006) 1878–1907.
- [18] H.M. Mourad, J. Dolbow, K. Garikipati, An assumed-gradient finite element method for the level set equation, *International Journal for Numerical Methods in Engineering* 64 (8) (2005) 1009–1032.
- [19] A. Hegab, T.L. Jackson, J. Buckmaster, D.S. Stewart, Nonsteady burning of periodic sandwich propellants with complete coupling between solid and gas phases, *Combustion and Flame* 125 (1) (2001) 1055–1070.
- [20] L. Massa, T.L. Jackson, J. Buckmaster, New kinetics for a model of heterogeneous propellant combustion, *Journal of Propulsion and Power* 21 (5) (2005) 914–924.
- [21] G.A. Holzapfel, J. Simo, Entropy elasticity of isotropic rubber-like solids at finite strains, *Computer Methods in Applied Mechanics Engineering* 132 (1–2) (1996) 17–44.
- [22] L. Vujosevic, V.A. Lubarda, Finite-strain thermoelasticity based on multiplicative decomposition of deformation gradient, *Theoretical and Applied Mechanics* 28–29 (2002) 379–399.
- [23] R. Malladi, J.A. Sethian, B.C. Vemuri, Shape modeling with front propagation: a level set approach, *IEEE Transactions on Pattern Analysis and Machine Intelligence* 17 (2) (1995) 158–175.
- [24] D. Adalsteinsson, J.A. Sethian, The fast construction of extension velocities in level set methods, *Journal of Computational Physics* 148 (1) (1999) 2–22.
- [25] N. Sukumar, D.L. Chopp, N. Moës, T. Belytschko, Modeling holes and inclusions by level sets in the extended finite-element method, *Computer Methods in Applied Mechanics Engineering* 190 (46–47) (2001) 6183–6200.
- [26] K. Matouš, P.H. Geubelle, Finite element formulation for modeling particle debonding in reinforced elastomers subjected to finite deformations, *Computer Methods in Applied Mechanics Engineering* 196 (1–3) (2006) 620–633.